CrossMark

Characterization of keyhole gas tungsten arc welded AISI 430 steel and joint performance optimization

Yan Xie [1,2] · Yangchuan Cai [1,2] · Xu Zhang [1,2] · Zhen Luo [1,2]

Abstract

Keyhole gas tungsten arc welding (K-TIG) is a recently developed welding process which enables single-pass welding without filler metal addition or joint preparation. Using K-TIG, 8-mm-thick AISI 430 ferritic stainless steel was successfully welded. The fusion zone of the weld was composed of columnar ferrite grains. Retained austenite was distributed along grain boundaries. The mechanical properties and corrosion resistance of the joint were tested. Three methods to enhance joint performance were trialed; high-frequency pulse arc welding (HFP-AW), austenite interlayer addition, and post-welding heat treatment (PWHT). Heat input was decreased by 42.24% when using HFP-AW. The addition of an austenite interlayer led to primary columnar austenite generation. Carbon precipitated and martensite diffused evenly into the matrix when using PWHT. The mechanical properties and corrosion resistance of the enhanced joints improved. In particular, the tensile properties of the PWHT joint and the corrosion resistance of the joint with the austenite interlayer were better than those of the base metal.

1 Introduction

Conventional gas tungsten arc welding (GTAW) is a clean, precise, and high-quality welding method. However, the welding current of GTAW is typically no higher than 250 A, making it unsuitable for welding thick plates. Additionally, the welding efficiency of GTAW is poor, limiting its potential applications. Keyhole welding methods, such as electron beam welding, laser welding, and plasma welding, are capable of welding thick plates efficiently. However, practical applications are limited because keyhole welding is unsuitable for on-site operation and is associated with high production costs.

Keyhole gas tungsten arc welding (K-TIG) was developed by the Commonwealth Scientific and Industrial Research

Organization (CSIRO) to address these problems with traditional keyhole welding methods. K-TIG was developed based on conventional GTAW [1]. Cooling water circulation was introduced in the constricting nozzle of the welding torch, and a higher welding current was adopted to increase the current density. The electromagnetically induced arc force is much higher in K-TIG than in GTAW. This force pushes the liquid metal in the molten pool outward, forming a keyhole [2]. The molten pool anchors itself to the root face of the weldment. The arc force, liquid metal density, and surface tension reach equilibrium, and this keeps the keyhole stable. K-TIG is capable of single-pass, full-penetration welding of thick plates. The welding equipment is based on a conventional GTAW power source and a specially designed welding torch. The equipment and production costs are low and the welding efficiency is very high. Additionally, K-TIG welding is suitable for on-site production.

K-TIG differs from plasma arc welding in several ways [3]. Plasma arc welding depends heavily on physical compression in the welding torch whereas a K-TIG arc ignites without physical compression. The diameter of the plasma arc is smaller than that of the electrode, whereas the diameter of the K-TIG arc is larger than that of the electrode. The molten pool in K-TIG welding is maintained and moved by arc force,

✉ Zhen Luo
lz@tju.edu.cn

1 School of Materials Science and Engineering, Tianjin University, 31-176, No.135 Yaguan Road, HaiHe Educational Park, Jinnan District, Tianjin 300072, China

2 Tianjin Key Laboratory of Advanced Joining Technology, Tianjin University, 31-176, No.135 Yaguan Road, HaiHe Educational Park, Jinnan District, Tianjin 300072, China
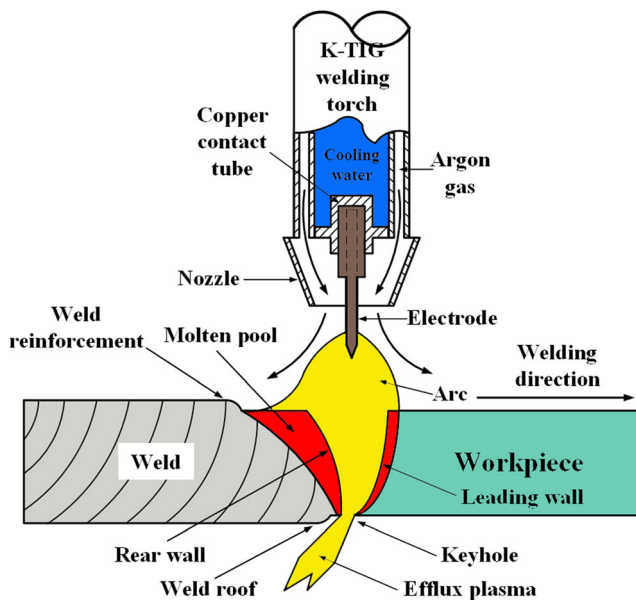
Fig. 1 Schematic of K-TIG process, the specially made torch, and the morphology of the molten pool

Table 1 Chemical composition of AISI 430 and AISI 304 (wt%)

Materials	Composition					
	Fe	Cr	Ni	C	Mn	Si
430	82	17	–	0.1	1	0.75
304	70	18	9	0.08	2	1

whereas recoil and stagnation collectively drive the plasma arc welding keyhole.

Previously, 12-mm-thick AISI 304 stainless steel and 12.7-mm-thick commercially pure titanium have been successfully welded using K-TIG in a single pass, without filler metal or joint preparation [2, 4]. Weld microstructures and mechanical performance were similar to those of conventional GTAW welds. Additionally, 10-mm-thick AISI 316L stainless steel has been successfully welded using K-TIG. Tensile and impact strengths reached 97 and 93.5%, respectively, of that of the base metal (BM) [5]. The corrosion resistance of the weld was also better than that of the BM. Water-cooled K-TIG has been successfully used to weld 8-mm Q345 plate. The heat input and weld volume were lowered. The resulting weldment had good mechanical properties [6].

More recently, constant-current DC conventional arc welding (CAW) has been applied to K-TIG. CAW uses a large heat input, leading to a large welding pool and heat-affected zone (HAZ). The core region arc plasma rate, arc force, penetrability, and energy density have been increased by adopting a high-frequency welding current [7, 8]. Furthermore, temperature and velocity distributions of the molten metal have been affected, the grain size decreased, and mechanical properties improved [9, 10]. A DC high-frequency welding power source can produce a high-frequency pulse current, increasing peak arc force, and decreasing heat input. High-frequency pulse arc welding (HFP-AW) is well suited to the K-TIG process.

Ferritic stainless steel (FSS) is widely used in automotive exhaust systems, heat exchangers, and water tanks. Owing to the absence of nickel, FSS has an economic advantage over austenitic stainless steel, increasing potential applications. However, coarse grains form in the fusion zone (FZ) and HAZ of weldments in FSS, lowering the ductility and impact toughness of the weldments. Therefore, improving the ductility and toughness of weldments is important in promoting applications for FSS.

Austenitic filler metal is used in production FSS welding to improve the mechanical properties of the weldment. However, the mechanism of this remains unclear, and different studies have reported different results. In one study, 10-mm-thick AISI430 FSS was welded using plasma arc welding with an AISI 316L austenitic stainless steel interlayer. The austenitic interlayer led to an increase of austenite and lath martensite in the FZ and a decrease in carbide precipitation formation and distribution. The ductility of the weldment improved significantly [11]. In a different study, AISI 21% Cr FSS was welded using pulsed GTAW with AISI 309L austenite stainless steel as an interlayer. The grain refined, and the weldment possessed almost full ferrite, improving the corrosion resistance

Fig. 2 Microstructure of AISI 430 FSS as delivery state

Table 2 Design matrix of CAW process parameters

Weld run	Current source	Welding current (A)	Welding speed (mm/min)	Arc voltage (V)
1	CAW	550	400	17.0
2	CAW	550	500	17.1
3	CAW	580	400	17.4
4	CAW	580	500	17.7
5	CAW	580	600	17.1
6	CAW	630	500	17.2
7	CAW	630	600	16.6

Table 3 Design matrix of the joint enhancement welding process parameters

Weld run	Current source	Interlayer addition	PWHT	Welding current (A)	Welding speed (mm/min)	Arc voltage (V)
8	HFP-AW	–	–	Base 200 Peak 470	500	16.8
9	CAW	With	–	580	400	17.2
10	CAW	–	With	580	600	17.1

of the joint. Further study is necessary to clarify the mechanism involved [12].

Post-welding heat treatment (PWHT) is an effective method to improve mechanical properties of a welded joint. However, there is little research available on PWHT for FSS weldments, because sensitization is regarded as the main flaw of PWHT for stainless steel. However, proper cooling rate control can be used to avoid sensitization. Annealing as a PWHT for 17% Cr FSS has been found to enable carbon and chromium to diffuse evenly, improving the mechanical properties of the welded joint [13]. Proper PWHT processes and detailed research into the mechanisms involved in welded FSS joints have great practical engineering value.

In the present study, 8-mm-thick AISI 430 FSS plate was welded using K-TIG. CAW was adopted. The microstructure and metallographic phases of the joint and the effects of welding parameters on weld appearance and performance were studied. Three enhancement methods were tested to optimize joint performance; HFP-AW, austenitic interlayer addition, and PWHT. The metallographic phases, mechanical properties, and corrosion resistance of
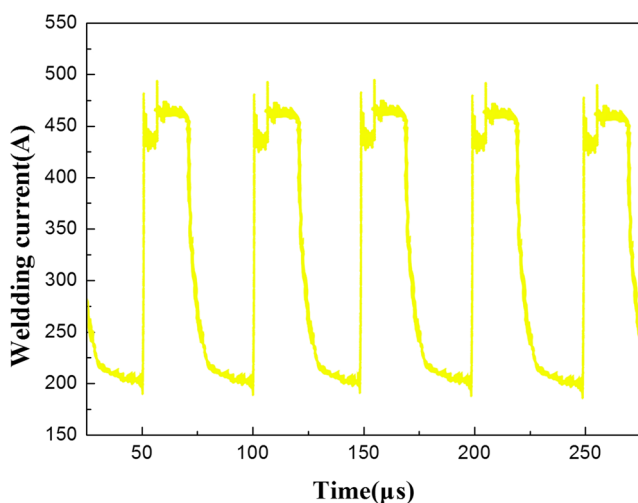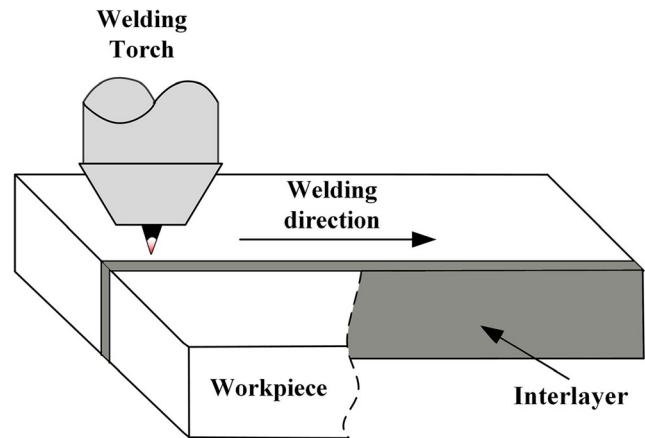

Fig. 4 Schematic of the interlayer addition position

the enhanced joints were studied. The mechanisms of the enhancements were also studied.

2 Experimental

Because of the large current capacity requirement, a specially designed K-TIG torch, equipped with a 6-mm-diameter tungsten electrode, was introduced. As Fig. 1 shows, a cooling water circulation system was set above the electrode, to increase current density and decrease electrode loss. A cooling water circulation system is necessary because the output current is up to 1000 A. A copper contact tube was set between the cooling water and electrode to enhance thermal conduction. A constant-current DC welding power source and a high-frequency inverter rectifier welding power source were used in the welding process. The shielding gas was pure argon supplied at 20 L/min. PWHT was performed with a heat-treatment furnace using air as the cooling medium.

The welding material was as-rolled AISI 430 FSS. The microstructure at room temperature was bamboo-like ferrite, shown in Fig. 2. The plates were cut into 210-mm × 150-mm × 8-mm samples. The welding surfaces were mechanically ground before welding to remove any oxide layer or impurities. A 2-mm-thick AISI 304 austenite stainless-steel sheet was used as an interlayer. The chemical compositions of AISI 430 and AISI 304 are presented in Table 1.
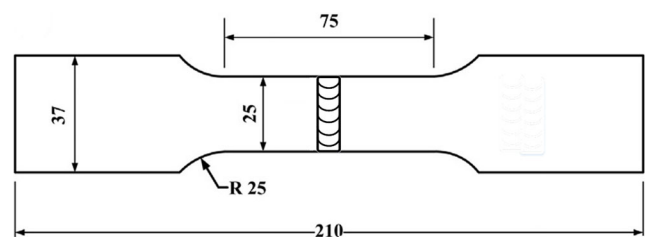

Fig. 3 Waveform of the HFP-AW current

Fig. 5 Schematic of tensile test specimen dimensions

The focus of the present study was mainly to compare joints produced by different optimum welding processes. Therefore, many prior experiments had been conducted to select the optimum performance parameters for each welding process. The optimum performance parameters were found to be different for different welding processes. Representative

welding parameters were also selected to show the performance variation trends.

The welding tests included two parts, which were the CAW process and the weld enhancement processes, respectively. The welding parameters of the CAW process are listed in Table 2. Neither interlayer addition nor PWHT was used. The welding

Fig. 6 Process window and the weld profile of the CAW joints. (a) The process window. (b)–(h) The weld profile: the numbers in the upper left corner of each picture correspond to the test number
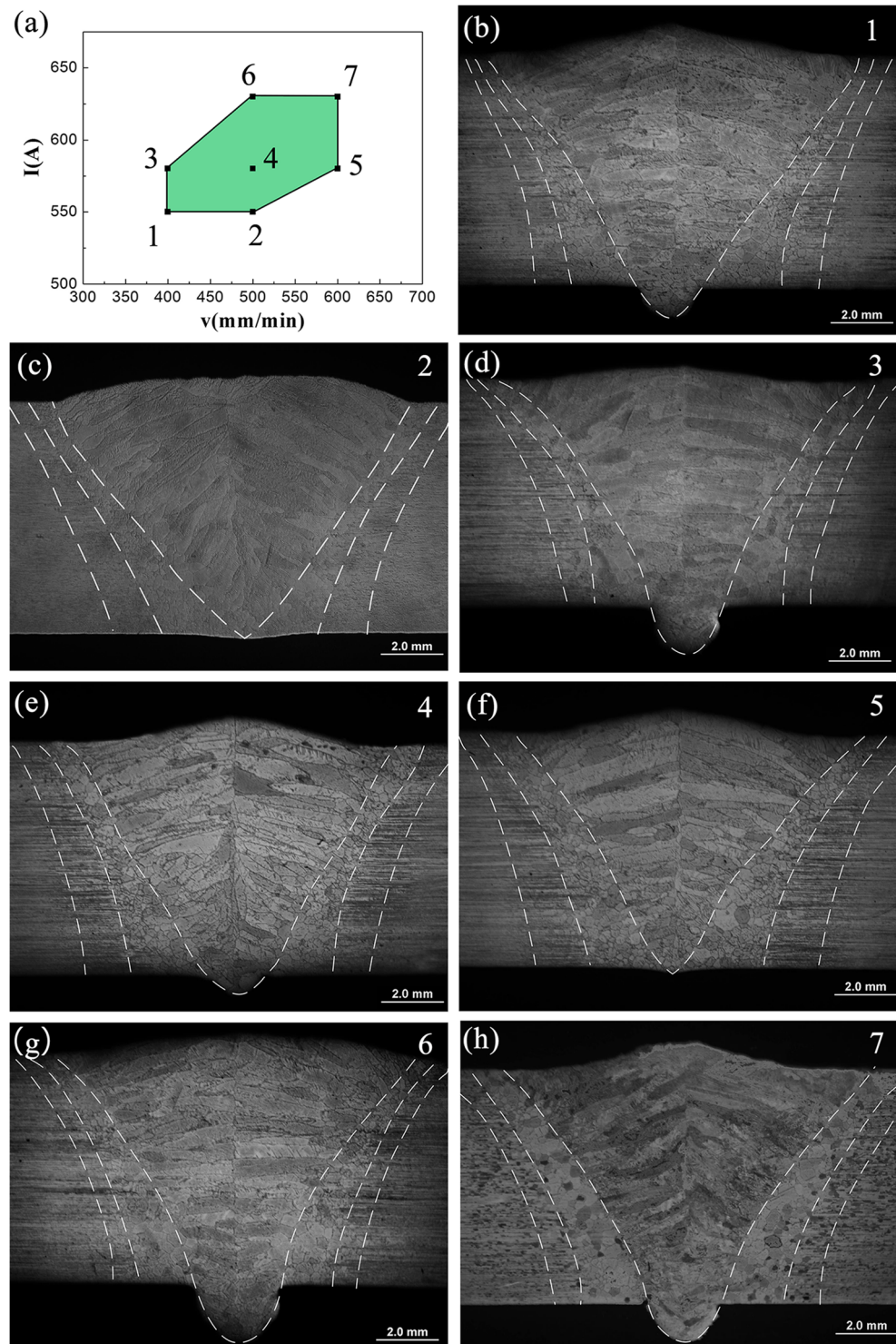
Table 4 EDS spot analysis result of CAW joint (%)

Element	Spot 1		Spot 2	
	Weight ratio	Atomic ratio	Weight ratio	Atomic ratio
C	2.82	11.76	9.28	32.00
Cr	14.71	14.19	13.44	10.71
Fe	82.47	74.05	77.28	57.30

parameters of the weld enhancement processes are listed in Table 3. In test 8, HFP-AW was used with pulse frequency 20 kHz, pulse period 50 μs, and duty ratio 50% (as shown in Fig. 3). In test 9, a constant welding current was used, and an AISI 304 interlayer was added. In test 10, PWHT was conducted on the CAW joint, with optimal performance as determined in the first part of this study (the CAW process). For annealing, the temperature was 800 °C, held for 20 min, and cooled in air.

Bead-on-plate welding was conducted in all tests except for test 9. A butt joint without preparation was used in test 9 because the interlayer was added. The schematic of the interlayer is shown in Fig. 4.

An Olympus optical microscope was employed to characterize the weld microstructure. The specimens were etched with Vilella's reagent, which contains 1 g picric acid, 5 mL hydrochloric acid, and 100 mL ethyl alcohol. The tensile tests were performed in accordance with GB/T2651-2008. The specimen dimensions are presented in Fig. 5.

Fracture morphology of the tensile test specimens was observed using a Hitachi 3400N scanning electron microscope. Potentiodynamic polarization tests were carried out on an electrochemical workstation with a three-electrode system in which the specimen, saturated calomel electrode, and platinum electrode were set as the working, reference, and auxiliary electrodes, respectively. 3.5%wt NaCl solution was used as the corrosive medium. The electrochemical tests were performed on the FZ, HAZ, and BM independently to investigate the corrosion behavior of each region of the joint. The sweep rate was set at 1 mV/s.

Table 5 Potentiodynamic polarization data of CAW joints

Test run	FZ		HAZ	
	I_{corr} (μA/m^2)	E_{corr} (V)	I_{corr} (μA/m^2)	E_{corr} (V)
1	0.050	− 0.36	0.016	− 0.26
2	0.025	− 0.42	0.023	− 0.35
3	0.040	− 0.38	0.021	− 0.24
4	0.040	− 0.36	0.023	− 0.40
5	0.063	− 0.33	0.022	− 0.39
6	0.036	− 0.37	0.022	− 0.38
7	0.023	− 0.38	0.021	− 0.37

Specimens were polished and cleaned with acetone before the experiments.

3 Results and discussion

3.1 Profile and performance of CAW joint

3.1.1 Effects of welding parameters on the weld profile

The keyhole stabilization and process window depend on current and welding speed [2]. It is important to investigate the process window and the weld profile. Full penetration is required and forming defects, such as undercut and porosity, must be avoided. The process window shows that high welding current is correlated with high welding speed (Fig. 6). Outside the process window, higher heat input (higher welding current or lower welding speed) generates excessive penetration and surface depression; lower heat input (lower welding current or higher welding speed) generates insufficient penetration. Figure 6 also shows the border between the FZ, high-temperature (HT) HAZ, low-temperature (LT) HAZ, and BM, and the molten pool, which is in the shape of a wine glass. The welding heat input is calculated by:

$$\text{HI} = \frac{\eta IV}{v} \tag{1}$$

where HI is the heat input; η is the process efficiency, which is constant for a certain welding process; I is the welding current; V is the arc voltage; and v is the welding speed. Since the process efficiency of K-TIG has not yet been calculated, the heat input was qualitatively compared in the present study.
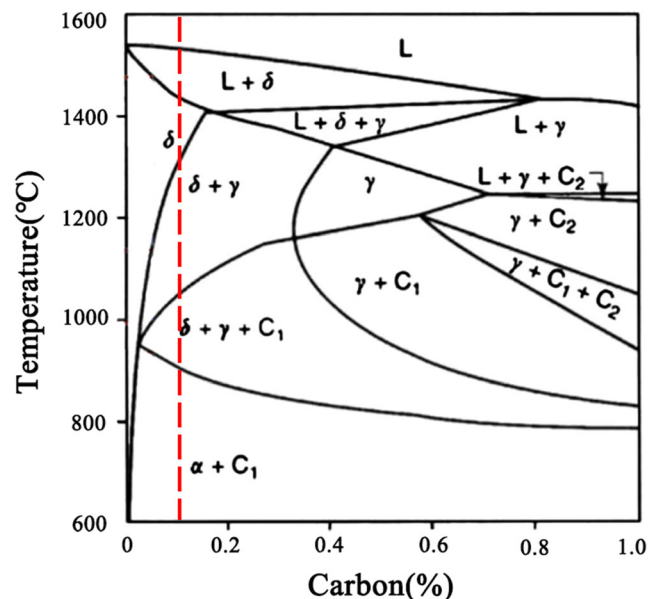

Fig. 7 Pseudo-binary diagram at 17% Cr [14]

Fig. 8 Microstructure of CAW joint. (a) Joint profile. (b) Enlarged view of the FZ. (c) Intergranular austenite. (d) Enlarged view of the HTHAZ. (e) Martensite precipitation in the HTHAZ. (f) Enlarged view of the LTHAZ. (g) Carbide precipitation in grain boundaries between austenite and ferrite. (h) Carbide precipitation in grain boundaries between ferrite matrices
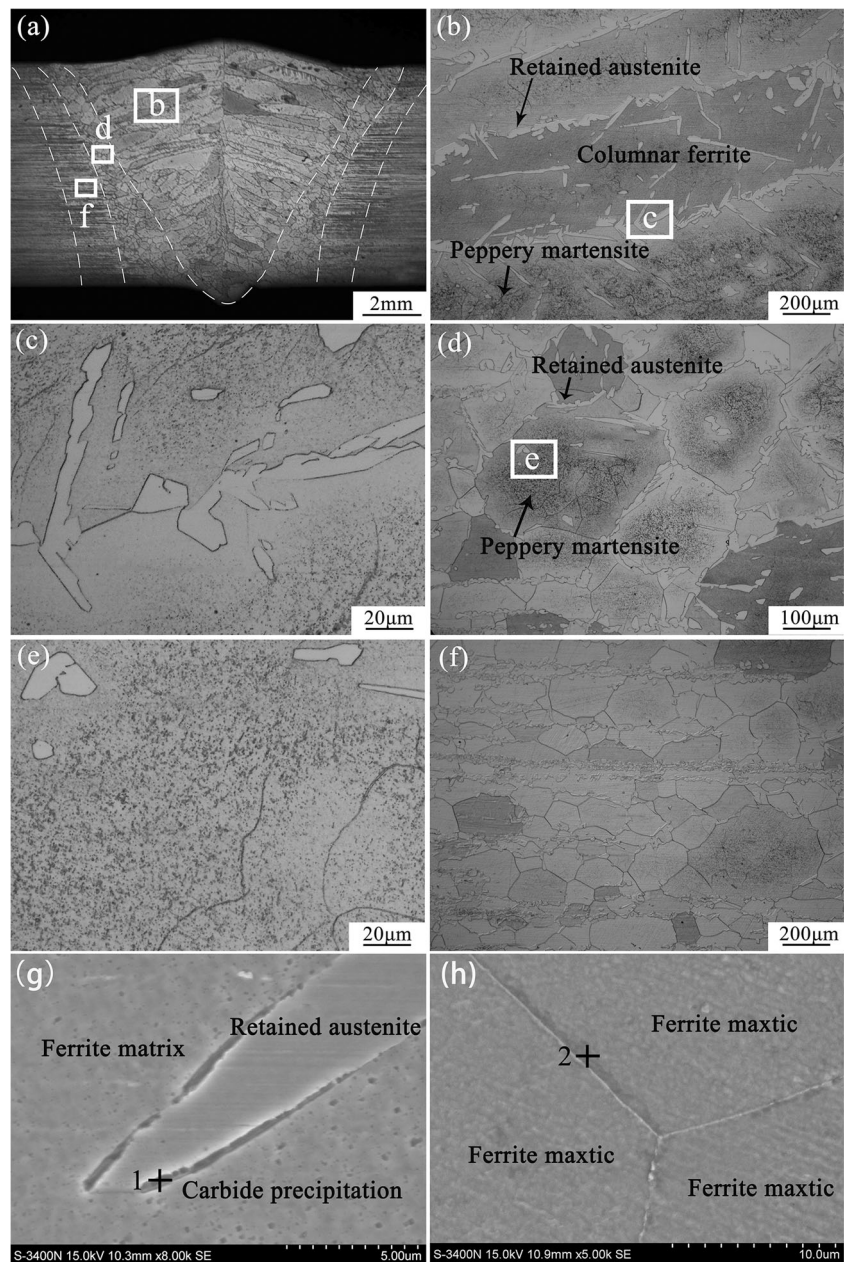
Sorting the tests by calculated heat input, from low to high, gives 5, 7, 2, 4, 6, 1, and 3. Though the heat input of test 2 is higher than that of test 7, the former barely penetrates, and the latter has a higher weld roof height. Similar phenomena exist in the comparison between test 1 and test 6. This is attributed to higher arc pressure generated by higher current. Higher welding parameters contribute to full penetration.

3.1.2 Microstructure of the CAW joint

Owing to the absence of nickel, the solidification mode of FSS is the F mode, which means the ferrite grains crystallize directly from the liquid metal. According to the pseudo-binary diagram [14], δ-ferrite was the first phase solidified from the liquid. Then, part of the δ-ferrite transformed into austenite, then carbide precipitation formed. Finally, the δ-ferrite and austenite transformed into α-ferrite. The phase composition at room temperature is α-ferrite and carbon precipitation.

Figure 8 shows the typical microstructure of the CAW joint; the profile of the FZ, HTHAZ, and LTHAZ was delineated by the white lines. The FZ consists of coarse columnar δ-ferrite grains which grow towards the upper part of the weld center, since this part is the final solidification position in the weld. Coarse columnar δ-ferrite grains were also reported in AISI 430 FSS joints welded using gas metal arc welding and TIG [15, 16].
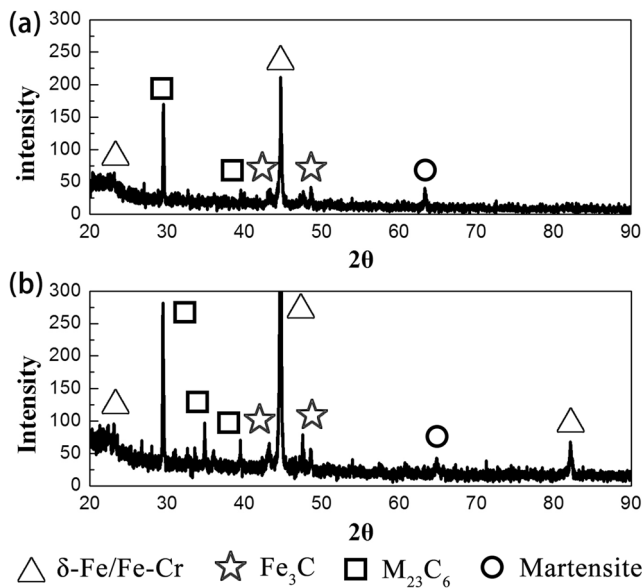
Fig. 9 XRD spectra of the CAW joint. (a) At the FZ. (b) At the HAZ

A small amount of austenite distributes at the ferrite grain boundaries. This austenite transforms from δ-ferrite during solidification and is defined as retained austenite. δ-Ferrite is the primary phase in solidification. The enriched concentration of carbon atoms, high distortion energy at grain boundaries, and intergranular segregation provides nucleation sites and nucleation energy for austenite. The retained austenite enhances the plasticity and toughness of the ferrite matrix [17, 18].

As shown in the enlarged views in Fig. 8(g) and (h), a kind of black phase distributes at the grain boundaries between austenite and ferrite, as well as between the ferrite matrices. According to energy dispersive spectroscopy (EDS) spot analysis (Table 4) and X-ray diffraction (XRD) spectra, carbon enriches in the black phase. The phase composition is chromium carbide precipitation and iron carbide precipitation which dissolves in the Fe-Cr solid solution matrix. However, the chromium content in the precipitation is lower than that in the base metal, which means the precipitation was not the product of sensitization and will not severely absorb the chromium in the matrix.

Martensite is distributed inside the ferrite grains and clusters as it precipitates. A similar behavior was observed in AISI 444

FSS joints [19]. The low distortion energy inside the grains and high cooling rate make it difficult for small austenite nuclei, which form in ferrite grains, to grow. Therefore, the granular austenite eventually transformed into martensite.

The HTHAZ is composed of coarsened equiaxed grains; the width of the HTHAZ is a few grains. Intergranular austenite and martensite are also observed in this region. Some grains in the LTHAZ recrystallize and turn into equiaxed grains from bamboo-like grains. The rest keep in the original shape. Little austenite and martensite were observed in the LTHAZ, because the heat input is insufficient. Some small grains distribute in lines and are parallel to the rolling direction. These grains grow from the tiny or fractured grains produced by rolling.

As Fig. 9 shows, the FZ is mostly composed of δ-ferrite and Fe-Cr solid solution, iron carbide, and chromium carbide precipitation were observed. Though the intensity peak for martensite is not strong, compared with metallographic observation, martensite does exist in the joint. The main phase composition was similar in the FZ and HAZ. The XRD result is consistent with metallographic observation.

3.1.3 Mechanical properties and corrosion resistance performance of the CAW joint

Figure 10 shows the effect of welding parameters on tensile properties. The optimal parameters are 580 A and 500 mm/min (test 4). With these welding conditions, the tensile strength reaches 59.2% of that of the BM (the tensile strength of BM is 497.1 MPa). The tensile curve is almost straight which means no obvious plastic deformation stage is observed. The tensile strength of 4-mm-thick AISI 409 FSS joints produced by shielded metal arc welding and gas metal arc welding reach 59 and 56%, respectively, of the BM [20]. The tensile strength of 3-mm-thick AISI 430 FSS joints produced by GTAW reach 61% of BM [21]. A K-TIG joint reaches the same tensile strength as the above welding processes. The CAW joint is suitable for small static loads. Otherwise, joint enhancement is necessary.

Fig. 10 (a) Effect of welding parameters on tensile properties. (b) Typical tensile curves of CAW joint and the BM
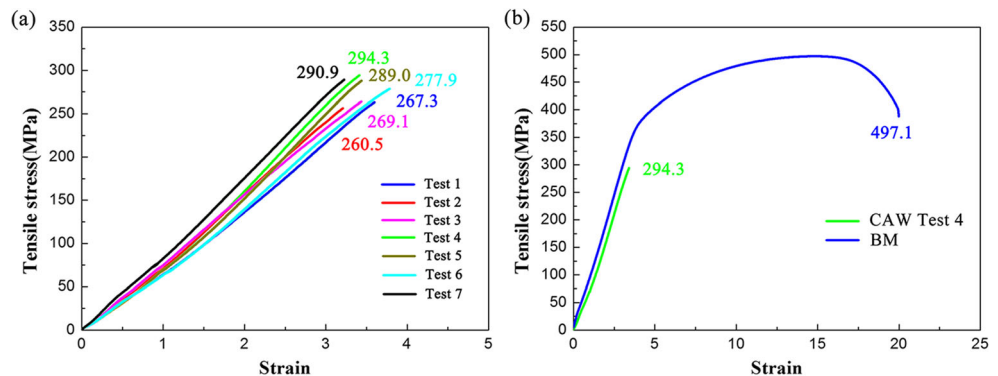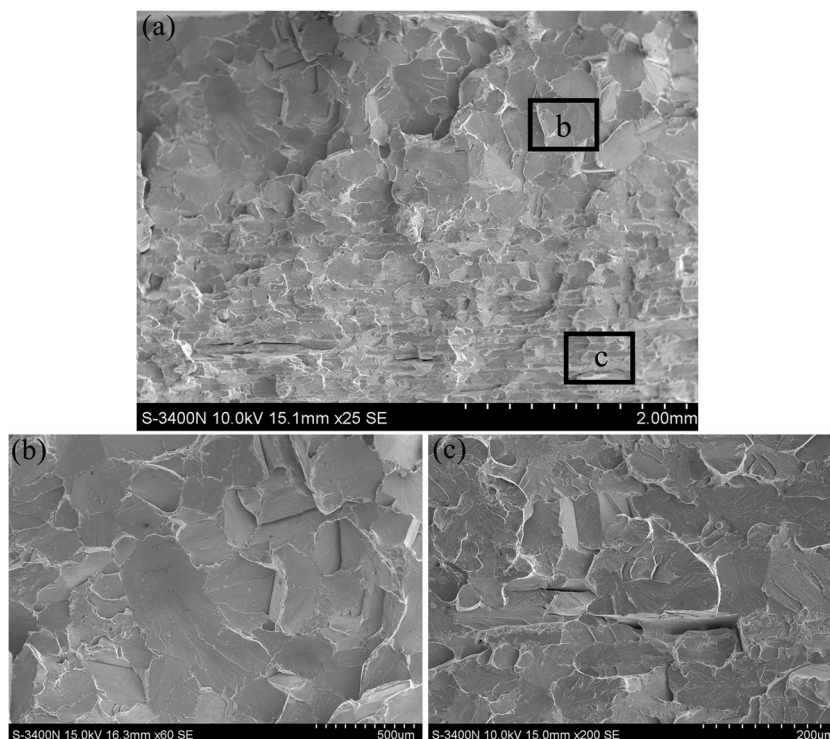
Fig. 11 Tensile fracture morphology. (a) Macro morphology. (b) Enlarged view of the upper region. (c) Enlarged view of the root region

A typical tensile test specimen fracture surface is shown in Fig. 11. Fracture occurs at the border between the FZ and HAZ. Two fracture regions are observed in all specimens; both regions exhibit cleavage fracture according to the enlarged view. However, the cleavage facet size in the upper region is remarkably larger than that in the root region. In contrast with the metallographic structure, the upper region belongs to the FZ and the root region belongs to the HTHAZ according to the difference of grain size. Different grain morphology leads to different elasticity modulus; stress concentrates in the border and a crack initiates. Then, the crack propagates perpendicular to the load, which accounts for the two regions in the fracture surface.

The potentiodynamic polarization curves are shown in Fig. 12. The corrosion current density (I_{corr}) and corrosion potential (E_{corr}) are presented in Table 5. The I_{corr} and E_{corr} of the BM are 0.050 $\mu A/m^2$ and -0.17 V, respectively. Test 7 has the lowest E_{corr} and I_{corr} among all the tests and has the optimal corrosion resistance. The E_{corr} of the FZ and HAZ is lower than that of the BM, resulting in higher corrosion propensity. However, the lowest I_{corr} is lower than that of the BM, resulting in a lower corrosion rate. The corrosion current density of the HAZ is obviously lower than that of the FZ, resulting in better corrosion resistance. The test data varies more substantially in the HAZ than in the FZ. Hence, corrosion resistance in the HAZ deserves more attention.

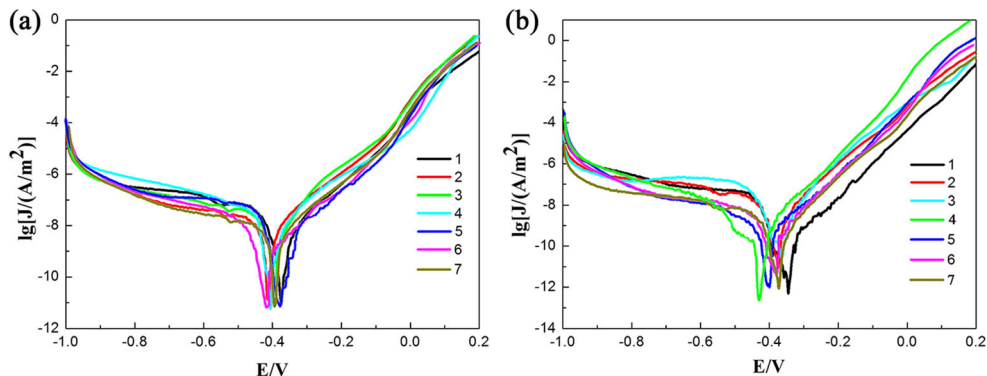**Fig. 12** Potentiodynamic polarization curves. (a) At the FZ. (b) At the HAZ

Fig. 13 Microstructure of HFP-AW joint. (a) The joint profile. (b) Enlarged view of the FZ. (c) Lamellar-type austenite and peppery martensite in the ferrite grains. (d) Enlarged view of the HTHAZ. (e) Enlarged view of the border between HTHAZ and BM
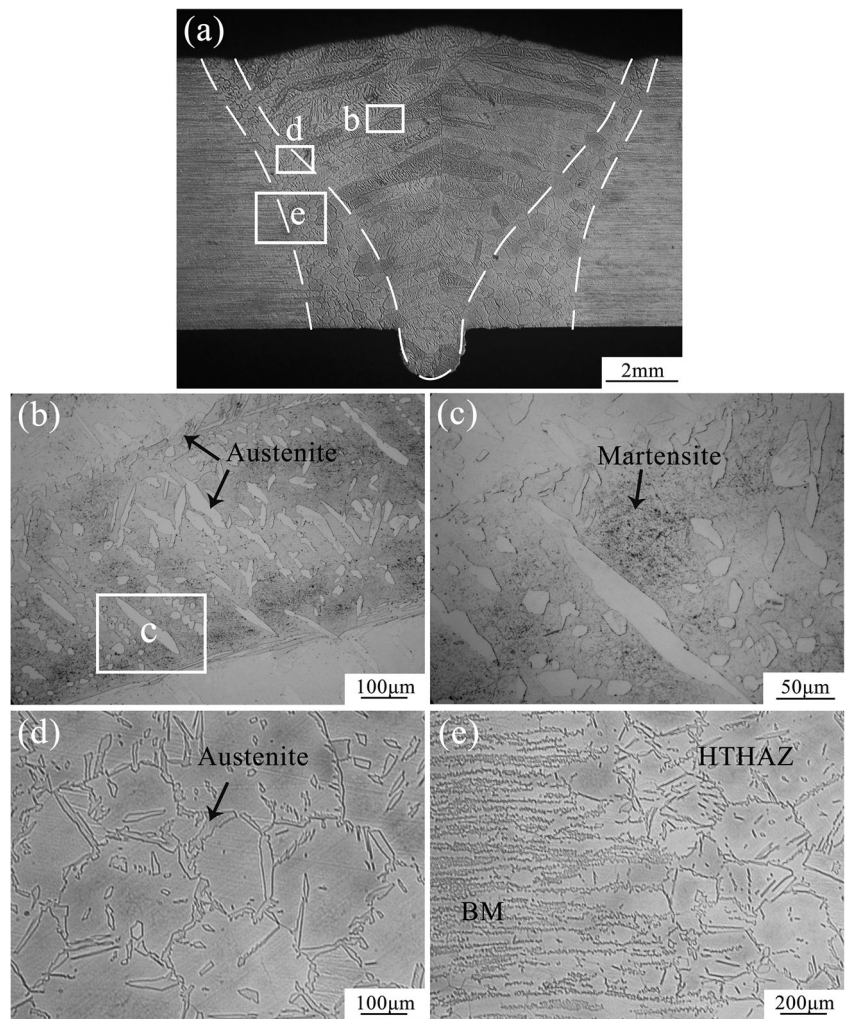

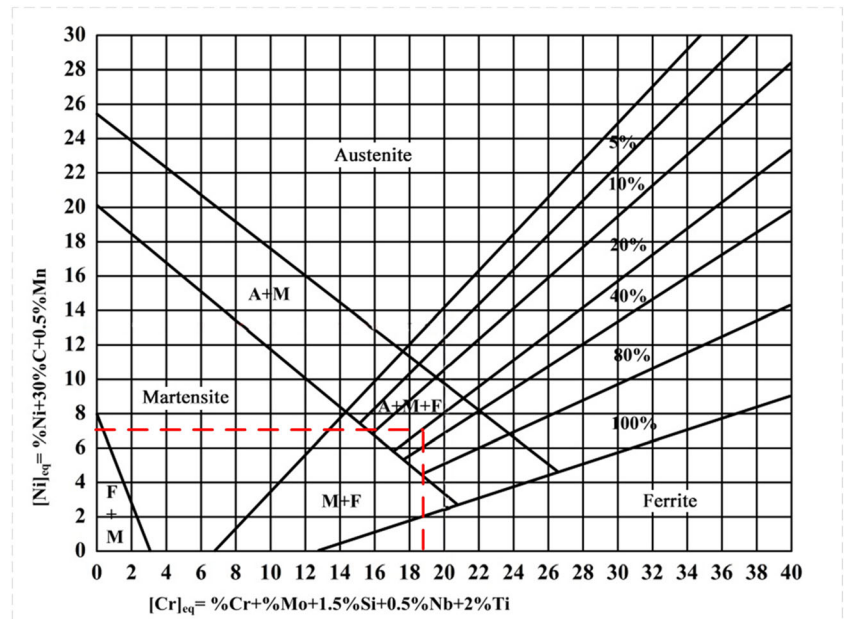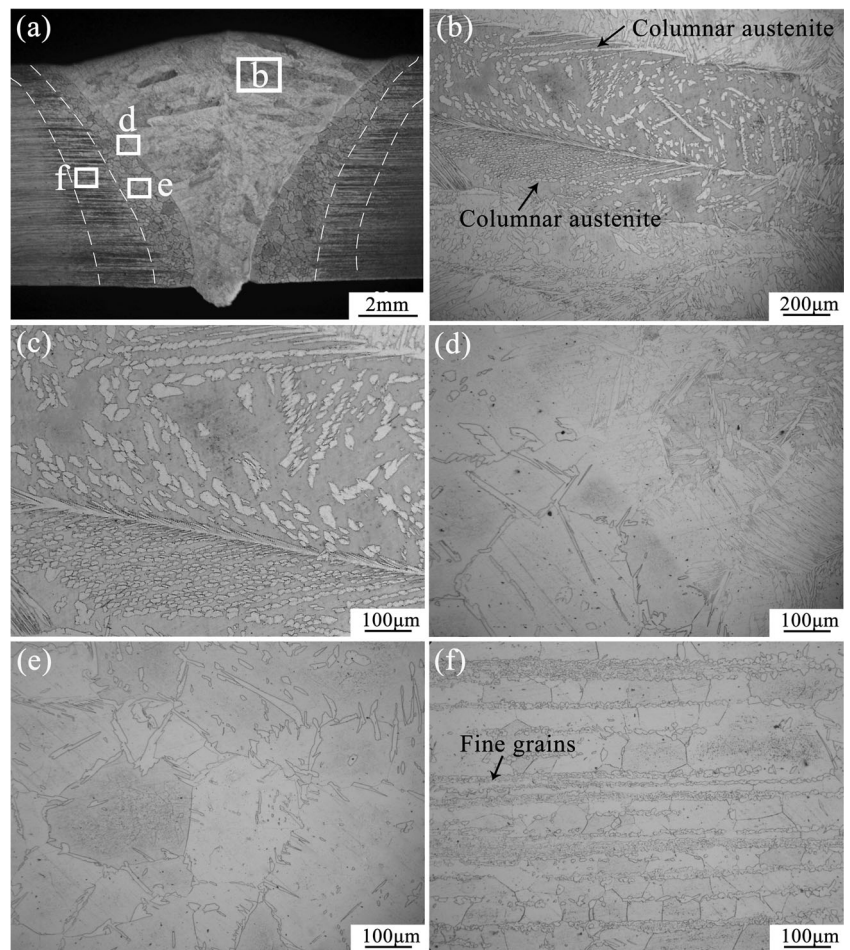**Fig. 14** The Schaeffler diagram

Fig. 15 Microstructure of the joint welded with interlayer. **a** Joint profile. **b** Enlarged view of the FZ. **c** Enlarged view of **b** showing columnar austenite in the ferrite grains. **d** The border between the FZ and HTHAZ. **e** Enlarged view of the HTHAZ. **f** Enlarged view of the LTHAZ

4 The effect of joint performance optimization processes

4.1 Microstructure of the enhancement process joints

4.1.1 Microstructure of the HFP-AW process joint

Figure 13 shows the joint microstructure of test 8. The peak current is smaller than the constant welding current when both fully penetrated. The heat input of HFP-AW, as calculated using Eq. 1, is 42.24% lower than that of the CAW joints.

The FZ consists of coarse columnar grains and martensite which distribute inside the ferrite grains. Fine austenite grains distribute both at the ferrite grain boundaries and inside the ferrite grains. The transgranular austenite grains are lamellar; the layers are perpendicular to both the growth direction of the ferrite grains and the temperature gradient. This is due to the solid-state phase transformation of austenite. Oversaturated carbon atoms in the matrix increase the distortion energy in the cooling and crystallization process. According to Fig. 7, austenite forms between 900 and 1300 °C. Since the temperature gradient in the weld is large, the austenite grains grow in

the lamellar shape. Low heat input and high cooling rate increased the austenite content in stainless steel alloys [22, 23].

The HTHAZ is composed of coarse equiaxed grains. Intergranular austenite is observed at the grain boundaries. As Fig. 13(e) shows, an obvious LTHAZ is not observed, which results from the low heat input. A narrow HAZ is considered beneficial for joint performance.

4.1.2 Microstructure of the interlayer added joint

Figure 14 shows the joint microstructure of test 9. The FZ is also composed of coarse columnar grains. The amount of austenite is remarkably larger than that in either the HFP-AW or CAW joint. The austenite is in the shape of columnar crystal and grows diagonally from the grain boundary to the inside. This austenite formation differs from the solid-state phase transformation in the CAW and HFP-AW joints. With the addition of nickel as an austenite stabilization element, the austenite solidifies directly from the liquid metal and grows along the temperature gradient, which leads to a columnar crystal morphology.

Fig. 16 Microstructure of PWHT joint. **a** Joint profile. **b** Enlarged view of the FZ. **c** Intergranular austenite after annealing. **d** Enlarged view of the HTHAZ. **e** Enlarged view of the LTHAZ. **f** Grains grown in the BM after annealing. **g** Morphology of austenite and carbide precipitation after annealing. **h** Enlarged view of carbide precipitation
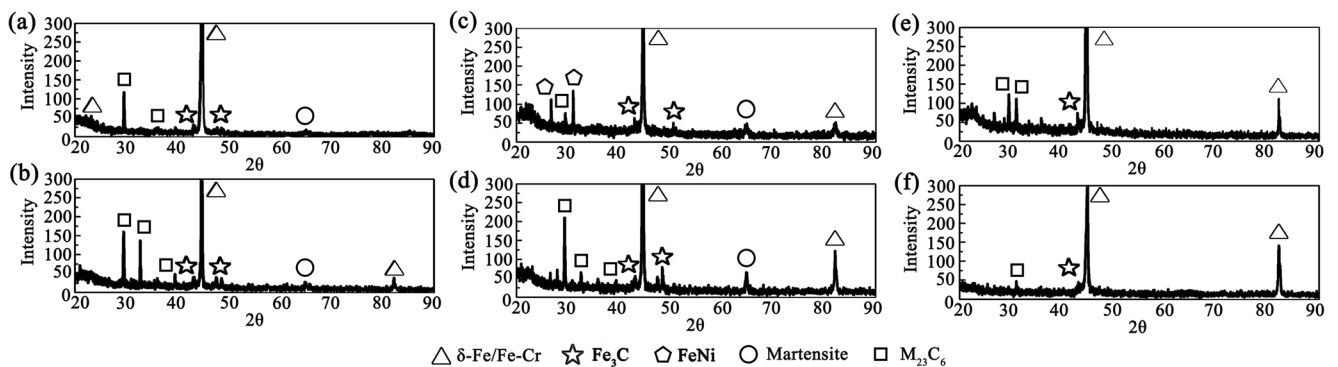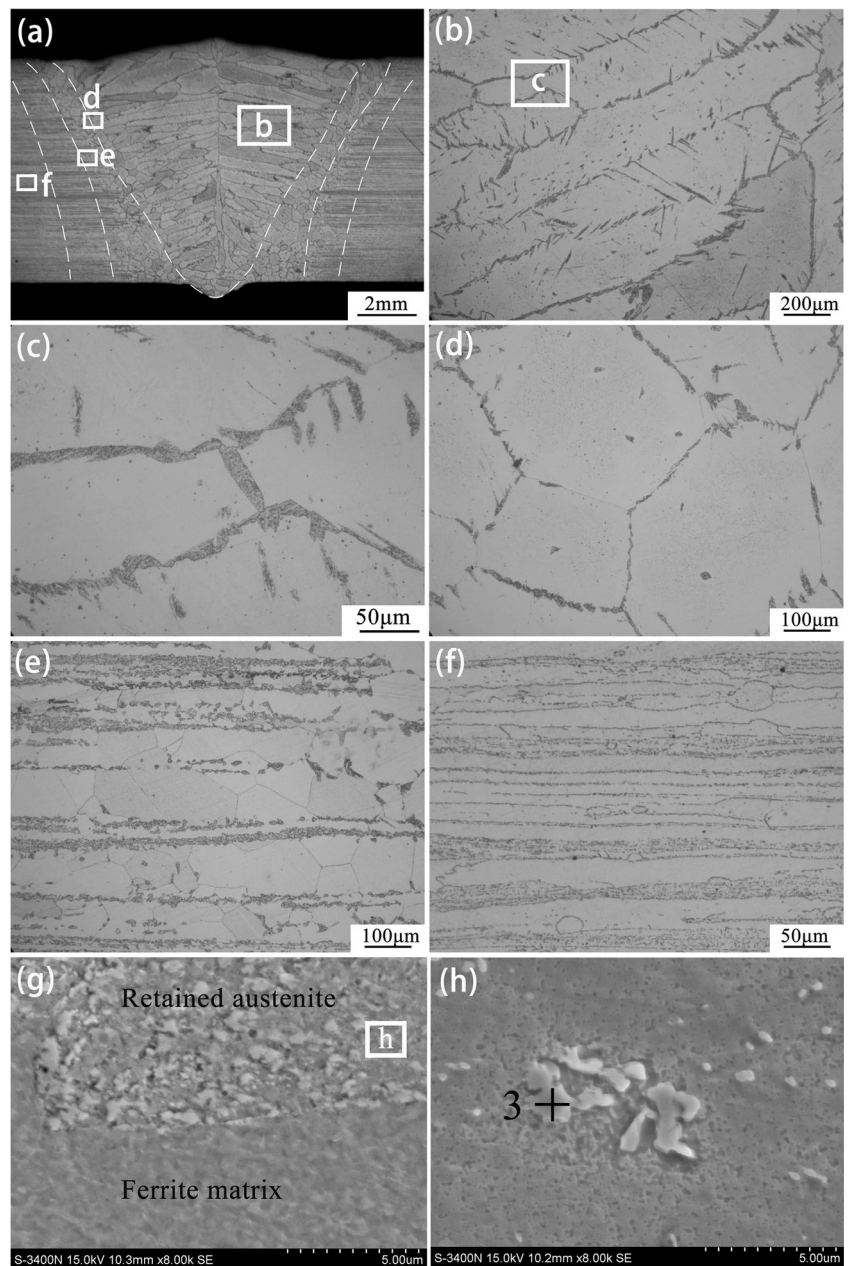

Fig. 17 XRD spectra. (a) HFP-AW weld. (b) HFP-AW HAZ. (c) Interlayer weld. (d) Interlayer HAZ. (e) PWHT weld. (f) PWHT HAZ

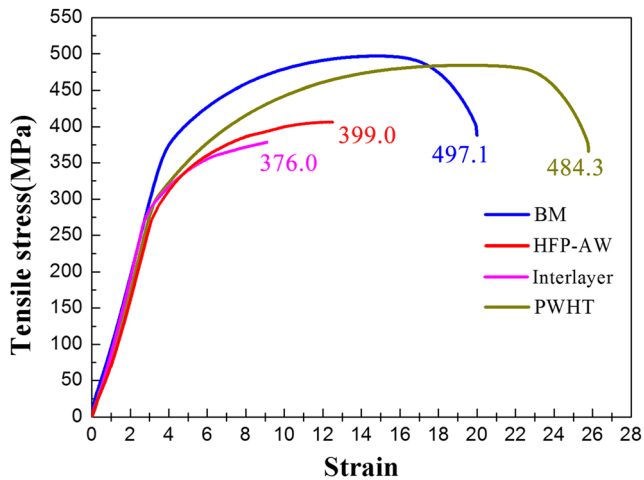△ δ-Fe/Fe-Cr   ☆ Fe₃C   ⬠ FeNi   ○ Martensite   ☐ M₂₃C₆

Fig. 18 Typical tensile curves of the enhancement process joints

Image analysis software is used to calculate the area of the weld, which is 46.74 mm². The area of the interlayer is 16 mm². The chemical composition of the weld is shown in Table 6.

The Schaeffler diagram can estimate the austenite content in the weld. The estimation depends on the ratio of the equivalent chrome $[Cr]_{eq}$ and equivalent nickel $[Ni]_{eq}$.

$$[Cr]_{eq} = Cr + Mo + 1.5Si + 0.5Nb = 18.7 \qquad (2)$$

$$[Ni]_{eq} = Ni + 0.5Mn + 30C = 6.5 \qquad (3)$$

The phase composition is shown in Fig. 14; the weld consists of 40% ferrite and 60% combined austenite and martensite. The amount of austenite is effectively improved.

The martensite content obviously decreases, which is attributed to the formation of primary austenite. Primary austenite absorbs supersaturated carbon which decreases the possibility of forming retained austenite, and consequently decreases the martensite.

The grain morphology and size in the HTHAZ and LTHAZ of the interlayer added joint are similar to that of the CAW joint. This results from the similar heat input of the two processes. A clear line is observed at the fusion line, as shown in Fig. 15(d). The grain structure on both sides of the line is continual. Different chemical compositions lead to different

Fig. 19 Tensile fracture morphology of the enhanced joints. (a) HFP-AW joint. (b) Enlarged view of (a). (c) Interlayer-added joint. (d) Enlarged view of (c). (e) PWHT joint. (f) Enlarged view of (e)
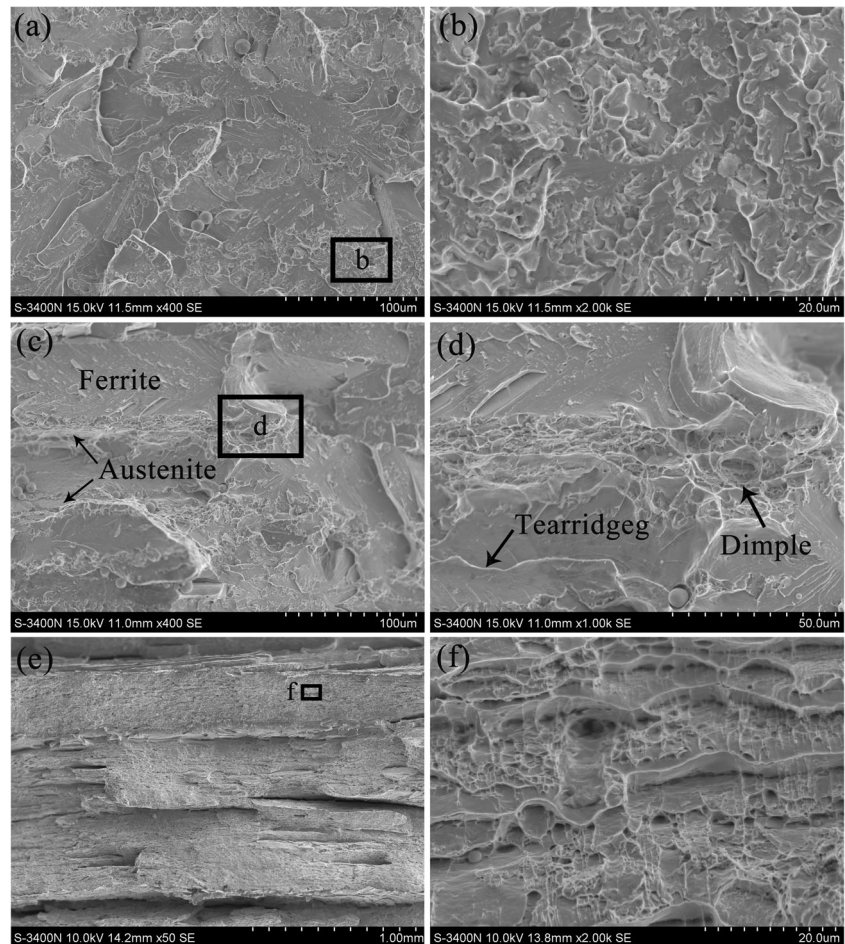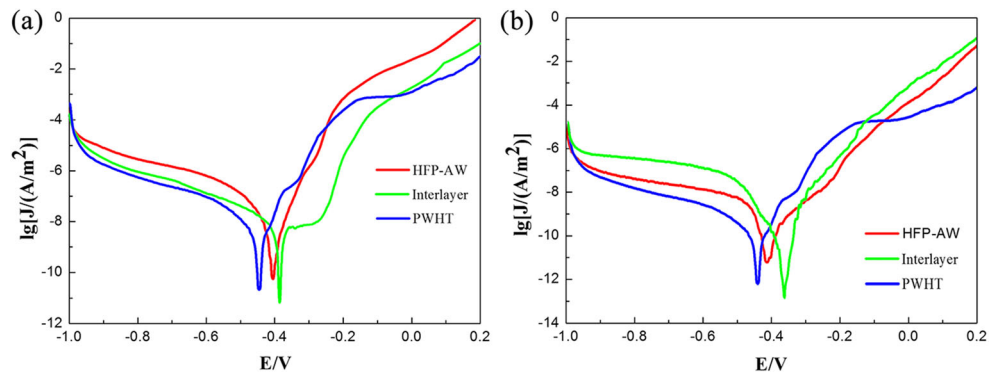
Fig. 20 Potentiodynamic polarization curves of specimens welded by the enhancement process joints. (a) At the FZ. (b) At the HAZ

corrosion resistance against etching solution, which may account for the emergence of the line.

4.1.3 Microstructure of the PWHT joint

A PWHT process was performed on the joint from test 4. As shown in Fig. 16, little change of grain morphology is observed. The austenite morphology turns into graininess, as shown in Fig. 16(g) and (h). As EDS spot analysis result, Table 7 shows the particles are enriched with carbide precipitation. The electric potential difference between carbide precipitation and matrix could degrade corrosion resistance performance. However, intergranular carbide precipitation is not observed because the carbide resolves in the PWHT process.

Few martensites are observed both in the FZ and HAZ. The annealing temperature is lower than the phase-transition temperature of austenite according to Fig. 7. According to metallographic observation and the XRD spectra shown in Fig. 17, no obvious σ-phase or χ-phase is observed. The chromium content in the precipitation is lower than that in the base metal. Therefore, precipitation was not the product of sensitization. Carbon and chromium diffuse evenly and martensite resolves after annealing, which accounts for the disappearance of martensite.

4.2 XRD phase analysis of the enhancement process joints

The phase compositions of the three enhancement process joints are mostly composed of δ-ferrite and Fe-Cr solid solution. Carbide precipitation is also observed in the three joints. Martensite is not observed in the PWHT joint. However, the interlayer-added joint contains a solid solution of Fe-Ni,

resulting from the addition of austenite interlayer. The XRD results are consistent with metallographic observation.

4.3 Mechanical properties of the enhancement process joints

Figure 18 shows typical tensile curves of the enhanced joints. Compared with CAW joint, the tensile strength and elongation rate of HFP-AW joint improve by 35.6 and 353.1%. According to the tensile curve, plastic deformation occurs before fracture, which indicates a remarkable improvement of plasticity. The increase of austenite content and decrease of HAZ width account for the enhancement of tensile properties. Since the smaller HAZ area means lower possibility for failure, it becomes difficult for cracks to extend in this area. Furthermore, the austenite lattice structure is face-centered cubic and has more slip systems than ferrite. The increase of austenite content increases the plasticity of the joint.

The tensile strength and elongation rate of the interlayer-added joint are 27.8 and 245.5% higher than those of the CAW joint, respectively. The increase of austenite content accounts for the enhancement of tensile properties.

The tensile strength and elongation rate of the PWHT joint are remarkably improved, reaching 97.4 and 131.0%, respectively, of those of the BM. The plasticity of the PWHT joint is better than the BM and the tensile fracture occurs on the BM. The PWHT process releases the internal stresses caused by rolling which results in tensile performance exceeding the BM.

Fracture morphologies of the enhanced joints are shown in Fig. 19. The fracture mode of the HFP-AW joint is brittle fracture. Tear ridge and river-like patterns are observed. The tear ridge is curly, and the facet size is smaller than the coarse grains,

Table 6 Chemical composition of the interlayer added joint (wt%)

Composition	Fe	Cr	Ni	C	Mn	Si
Content	77.9	17.4	3.1	0.09	1.3	0.84

Table 7 EDS spot analysis results of PWHT joint (%)

Elements	Weight ratio	Atomic ratio
C	6.07	22.93
Cr	13.50	11.78
Fe	80.42	65.30

which results from the increase of austenite content. The intragranular austenite hampers the extension of fractures, leading to cracks expanding along different cleavage planes and absorbing more fracture energy. The fracture mode of the interlayer-added joint is mixed. The ferrite grains show brittle fracture, whereas the austenite grains along the ferrite boundaries show ductile fracture and dimples are observed. The increase of austenite improved the plasticity of the joint. In contrast, the fracture in the PWHT joint sample occurs at the BM. Because the BM is as-rolled, the macromorphology is lamellar. The fracture surface clearly shows dimple-ductile fracture.

4.4 The corrosion resistance performance of the enhancement process joints

As Fig. 20 and Table 8 show, the corrosion resistance of the HFP-AW joint has no obvious improvement compared with those of the CAW joint, which results from the similar phase composition of the joints. The I_{corr} of the PWHT joint is obviously higher than that of other specimens, which means a higher corrosion rate. The corrosion resistance degrades after PWHT. Owing to the potential difference between the carbon precipitation and the matrix, the increase of carbon precipitation after PWHT increases the corrosion rate. Furthermore, the precipitation absorbs the adjacent chromium atoms and decreases the corrosion resistance. According to the EDS analysis in Table 7, since sensitization is not severe in the joint, the increase of carbon precipitation is the main cause of the performance degradation.

The addition of an austenite interlayer remarkably improves corrosion resistance. Passivation is observed; passivation potential is − 0.44 V, and the passivity current is 0.02 μA/m². The I_{corr} is lower than that of the BM and other specimens. However, the E_{corr} of all the specimens is higher than that of the BM. This indicates the corrosion rate of the joints is lower than that of the BM, but it is easier for the joints to start to corrode. The corrosion current density of the HAZ is obviously lower than that of the FZ, resulting in better corrosion resistance in the HAZ than in the FZ. Hence, the FZ performance enhancement of adding an austenite interlayer benefits corrosion resistance of the whole joint.

Table 8 Potentiodynamic polarization data of the enhancement process joints

Test run	FZ		HAZ	
	I_{corr} (μA/m²)	E_{corr} (V)	I_{corr} (μA/m²)	E_{corr} (V)
8	0.025	− 0.46	0.031	− 0.37
9	0.013	− 0.43	0.005	− 0.33
10	0.251	− 0.46	0.122	− 0.57

5 Conclusion

1. K-TIG was successfully applied to 8-mm-thick AISI 430 FSS. High welding current is correlated with high welding speed. FZ, HTHAZ, and LTHAZ were observed in the CAW joint. The FZ was composed of δ-ferrite, intergranular austenite, and martensite.

2. The optimal tensile strength of CAW joint reached 59.2% of that of the base metal, and achieved the same strength as shielded metal arc welding, gas metal arc welding, and GTAW. The tensile fracture surface exhibited cleavage fracture. Compared with the BM, corrosion resistance of the CAW joint degraded.

3. Compared with CAW, the heat input of HFP-AW decreased by 42.24%. The LTHAZ was negligibly small. The tensile strength and elongation were 35.6 and 353.1% higher, respectively, than those of the CAW joint. However, corrosion resistance of the HFP-AW joint had no obvious improvement.

4. The tensile strength and elongation rate of the interlayer-added joint were 27.8 and 245.5% higher, respectively, than those of the CAW joint. A large amount of columnar austenite distributed inside the ferrite grains. Corrosion resistance of the interlayer added joint was remarkably improved. The increased austenite content accounts for the enhancement of the tensile properties.

5. Martensite dissolved and austenite became grainy in the PWHT joint. The tensile strength and elongation rate reached 97.4 and 131.0%, respectively, compared with those of the BM. The plasticity of the PWHT joint was better than that of the BM. However, the corrosion resistance of the PWHT joint was significantly lower, because of the increased carbide precipitation in the austenite grains.

References

1. Jarvis B J (2001) Keyhole gas tungsten arc welding: a new process variant. Dissertation, University of Wollongong

2. Lathabai S, Jarvis BL, Barton KJ (2008) Keyhole gas tungsten arc welding of commercially pure zirconium. Sci Technol Weld Join 13:573–581. https://doi.org/10.1179/136217108X329296

3. Jarvis BL, Ahmed NU (2000) Development of keyhole mode gas tungsten arc welding process. Sci Technol Weld Join 5:21–27. https://doi.org/10.1179/136217100322910624

4. Lathabai S, Jarvis BL, Barton KJ (2001) Comparison of keyhole and conventional gas tungsten arc welds in commercially pure titanium. Mater Sci Eng A 299:81–93. https://doi.org/10.1179/136217108X329296

5. Feng Y, Luo Z, Liu Z, Li Y, Luo Y, Huang Y (2015) Keyhole gas tungsten arc welding of AISI 316L stainless steel. Mater Design 85: 24–31. https://doi.org/10.1016/j.matdes.2015.07.011

6. Fan W, Ao S, Huang Y, Liu W, Li Y, Feng Y, Luo Z, Wu B (2017) Water cooling keyhole gas tungsten arc welding of HSLA steel. Int J Adv Manuf Tech 92:1–10. https://doi.org/10.1007/s00170-017-0234-0

7. Yang M, Zheng H, Qi B, Yang Z (2017) Effect of arc behavior on Ti-6Al-4V welds during high frequency pulsed arc welding. J Mater Process Technol 243:9–15. https://doi.org/10.1016/j.jmatprotec.2016.12.003

8. Qi BJ, Yang MX, Cong BQ, Liu FJ (2013) The effect of arc behavior on weld geometry by high-frequency pulse GTAW process with 0Cr18Ni9Ti stainless steel. Int J Adv Manuf Technol 66:1545–1553. https://doi.org/10.1007/s00170-012-4438-z

9. Farzadi A, Serajzadeh S, Kokabi AH (2008) Modeling of heat transfer and fluid flow during gas tungsten arc welding of commercial pure aluminum. Int J Adv Manuf Technol 38:258–267. https://doi.org/10.1007/s00170-007-1106-9

10. Tarng YS, Yang WH (1998) Optimization of the weld bead geometry in gas tungsten arc welding by the Taguchi method. Int J Adv Manuf Technol 14(8):549–554. https://doi.org/10.1007/BF01301698

11. Teker T (2013) The effect of austenitic interlayer on microstructure and mechanical behaviors in keyhole plasma transfer arc welding of ferritic stainless steel couple. Int J Adv Manuf Technol 69:1833–1840. https://doi.org/10.1007/s00170-013-5158-8

12. Wu W, Hu S, Shen J, Ma L, Han J (2015) Sensitization of 21% Cr ferritic stainless steel weld joints fabricated with/without austenitic steel foil as interlayer. J Mater Eng Perfrom 24:1505–1515. https://doi.org/10.1007/s11665-015-1409-1

13. Castro ALR (1984) Effects of post-welding heat treatments on 17% chromium ferritic stainless steels. Dissertation, Associacao Brasileira de Metais

14. Lippold JC, Kotecki DJ (2005) Welding metallurgy and weldability of stainless steels. John Wiley & Sons, Hoboken, p 376

15. Srinivasan BP, Kumar SMP (2013) Characterisation of microstructure and corrosion behaviour of thin section AISI 430 stainless steel gas tungsten arc weldment. Soc Sci Med 44:137–143. https://doi.org/10.1179/174327808X286464

16. Ramkumar KD, Chandrasekhar A, Singh AK, Ahuja S, Agarwal A, Arivazhagan N, Rable AM (2015) Comparative studies on the weldability, microstructure and tensile properties of autogeneous TIG welded AISI 430 ferritic stainless steel with and without flux. J Manuf Process 20:54–69. https://doi.org/10.1016/j.jmapro.2015.09.008

17. Herrera C, Ponge D, Raabe D (2011) Design of a novel Mn-based 1 GPa duplex stainless TRIP steel with 60% ductility by a reduction of austenite stability. Acta Mater 59:4653–4664. https://doi.org/10.1016/j.actamat.2011.04.011

18. Zhou W, Guo H, Xie Z, Wang X, Shang C (2013) High strength low-carbon alloyed steel with good ductility by combining the retained austenite and nano-sized precipitates. Mater Sci Eng A 587:365–371. https://doi.org/10.1016/j.msea.2013.06.022

19. Silva CC, Farias JP, Miranda HC, Guimaraes RF, Menezes JWA, Neto MAM (2007) Microstructural characterization of the HAZ in AISI 444 ferritic stainless steel welds. Mater Charact 59:528–533. https://doi.org/10.1016/j.matchar.2007.03.011

20. Lakshminarayanan AK, Shanmugam K, Balasubramaniam V (2009) Effect of welding processes on tensile and impact properties, hardness and microstructure of AISI 409M ferritic stainless steel joints fabricated by duplex stainless steel filler metal. Ironmak Steelmak 16:66–72. https://doi.org/10.1179/174328108X378224

21. Mohandas T, Reddy GM, Naveed M A comparative evaluation of gas tungsten and shielded metal arc welds of a "ferritic" stainless steel. J Mater Process Technol 94:133–140. https://doi.org/10.1016/S0924-0136(99)00092-8

22. Alizadeh M, Marashi SPH, Pouranvari M (2013) Resistance spot welding of AISI 430 ferritic stainless steel: phase transformations and mechanical properties. Mater Design 56:258–263. https://doi.org/10.1016/j.matdes.2013.11.022

23. Elmer JW, Allen SM, Eagar TW (1989) Microstructural development during solidification of stainless steel alloys. Metall Mater Trans A 20:2117–2131. https://doi.org/10.1007/BF02650298